Ultracapacitor Assisted Powertrains: Modeling, Control, Sizing, and the Impact on Fuel Economy

Dean Rotenberg, Ardalan Vahidi, *Member, IEEE*, and Ilya Kolmanovsky, *Fellow, IEEE*

***Abstract*—This paper considers modeling and energy management control problems for an automotive powertrain augmented with an ultracapacitor and an induction motor. The ultracapacitor-supplied motor assists the engine during periods of high power demand. The ultracapacitor may be recharged via regeneration during braking and by the engine during periods of low power demand. A reduced-order model and a detailed simulation model of the powertrain are created for control design and evaluation of fuel economy, respectively. A heuristic rule-based controller is used for testing the impact of different component combinations on fuel economy. After a suitable combination of engine, motor, and ultracapacitor sizes has been determined, a model predictive control strategy is created for power management which achieves better fuel economy than the rule-based approach. Various component sizing and control strategies tested consistently indicate a potential for 5% to 15% improvement in fuel economy in city driving with the proposed mild hybrid powertrain. This order of improvement to fuel economy was confirmed by deterministic dynamic programming which finds the best possible fuel economy.**

***Index Terms*—Energy management, dynamic programming, hybrid vehicle, model predictive control (MPC), ultracapacitor.**

I. INTRODUCTION

PERIODS of quick acceleration require a much higher power output from an automobile than what is encountered under more typical driving conditions. A simple back-of-the-envelope kinetic energy calculation can show that accelerating a 2000 kg vehicle (roughly the size of a Ford Explorer SUV) from 0 to 60 m/hr (0 to 26.82 m/s) in 10 s requires an average of 70 kW of power, in addition to the power needed to overcome road and air drag forces. Almost the same amount of additional power (70 kW) is needed during a 1 s accelerator pedal tip-in to increase the velocity of that same vehicle from 45 to 48 m/hr. Situations such as these may consume a disproportionately high amount of fuel, and have a negative impact on the fuel economy of the vehicle. In conventional powertrains, the engine is typically sized much larger than needed for steady-state operation, in order to meet these spikes in power demand. In addition to the higher cost of a larger engine, operating a large combustion engine at its most efficient torque-speed combination is less likely during normal cruise.

This problem is answered in part by the current generation of hybrid vehicles, which run their (typically smaller) combustion engines more efficiently by utilizing the assistance of electric motors and battery packs for energy buffers. In addition, by recovering a portion of their kinetic energy through the use of electromagnetic regenerative braking, they are able to make that energy available to assist propulsion of the vehicle, saving a considerable amount of fuel. Among the remaining challenges in the field are the added cost and weight of large battery packs, the low cycle life of current available batteries, and the limited power release rate inherent in a battery, which makes a battery-powered electric motor unable to follow rapid power demand spikes without drastically increasing battery size and cost [1].

Rapid transients in power demand will be better handled by the use of high power density ultracapacitors [1], [2]. A typical ultracapacitor is capable of releasing or storing energy roughly ten times faster than a battery of the same weight. The total energy which it can store, however, is typically ten times less than that same battery, meaning that an ultracapacitor provides an order of magnitude increase in power density at the cost of an order of magnitude of energy density [3].[1] An ultracapacitor shares several of the basic characteristics of a normal capacitor. The electrodes are typically constructed by applying a layer of activated carbon to a layer of metal foil. The electrodes are submersed in an electrolytic fluid, and separated by a thin separator which acts as an electronic insulator between the electrodes and a conduit for ion transport. As charge builds up on the electrodes, ions from the solution are attracted to the surface of the activated carbon. This configuration is known as the electric double-layer capacitor. The powder-like carbon layer possesses a surface area far greater than that of a typical capacitor electrode, rising as high as 375 000 m^2 for just 250 g of carbon, and the membrane provides a charge separation which can be as low as a few nanometers.[2] These characteristics enable a capacitance on the order of 1000–5000 F [3], [2],[2] several orders of magnitude greater than that of a conventional capacitor. Despite this increased capacitance, the energy density of the ultracapacitor is still substantially lower than that of a battery. However, the serial resistance of an ultracapacitor is multiple times lower than a battery's resistance, typically less than 1 mΩ [4],

Manuscript received April 13, 2009; revised March 02, 2010; accepted March 24, 2010. Manuscript received in final form April 12, 2010. Recommended by Associate Editor S. Liu. This work was supported by research grants from Ford Research and Advanced Engineering and U.S. Army Tank Automotive Research, Development and Engineering Center (TARDEC).

D. Rotenberg and A. Vahidi are with the Department of Mechanical Engineering, Clemson University, Clemson, SC 29634 USA (e-mail: drotenb@clemson.edu; avahidi@clemson.edu).

I. V. Kolmanovsky is with the Department of Aerospace Engineering, The University of Michigan, Ann Arbor, MI 48109-2140 USA (e-mail: ilya@umich.edu).

Digital Object Identifier 10.1109/TCST.2010.2048431

[1][Online]. Available: http://www.maxwell.com

[2][Online]. Available: http://ffden-2.phys.uaf.edu/212_spring2005.web.dir/mike_wright/index.html

Fig. 1. 48 V BMOD0140 Maxwell ultracapacitor module with capacitance of 140 F (Dimensions 41.6 × 19 × 16 cm, Mass ≈ 13.6 kg). While the maximum total energy stored is a mere 161 kJ, this energy can be released in just a few seconds generating considerable power boost to a vehicle. The maximum power for this product is 4800 W per unit mass or almost 65 kW instantaneous maximum power. Newer products listed on Maxwell website[1] have even higher power densities.

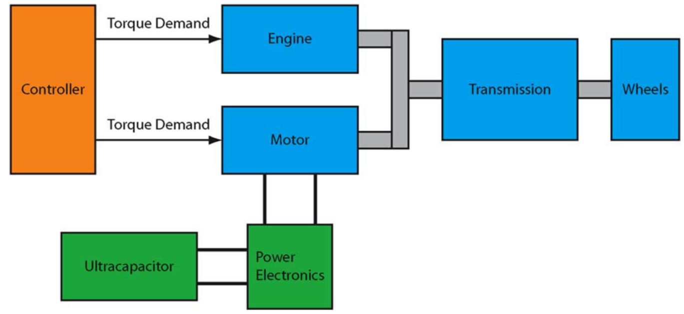

Fig. 2. Overview of the structure of a parallel hybrid with ultracapacitor energy storage.

[5]. This low resistance allows for a much higher current to be drawn, giving an ultracapacitor a much higher power density. It is the combination of high power density and low energy density and their reliable [6] operation which makes the ultracapacitor well-suited to accommodating brief power demand spikes. Other advantages of the ultracapacitor include a very high cycle life, on the order of more than 500 000 cycles [1]–[3], [4], [5], and the ability to operate over a wide range of temperatures, providing consistent performance at temperatures as low as −40 °C [5]. Maxwell Technologies,[1] a main provider of ultracapacitors in North America, has been introducing new models over the last few years that have higher power densities and reduced cost (see Fig. 1). Because of the properties which differentiate them from batteries, high power-density ultracapacitors may be integrated with vehicle powertrains (in a mild parallel hybrid configuration) to boost available power during vehicle acceleration and relax engine transients, making them an effective mechanism for reducing fuel consumption and emission levels without compromising vehicle agility [3], [2]. Moreover, in many situations, regenerative braking alone may provide sufficient energy for this power boost [7]. The additional cost and weight of the ultracapacitor and electric motor may be justified by a downsized internal combustion engine and, since transients the engine is exposed to are reduced, even possibly by a less costly catalytic converter.

While full hybrid vehicles, which rely on batteries for power leveling, have reached mass production, the use of ultracapacitors in mild hybrids remains a technology to explore. Most of the existing research on ultracapacitor hybrids is geared towards transit buses where their frequent stop-and-go cycle match the operational characteristics of ultracapacitors [8]–[10]. Some researchers have proposed use of ultracapacitors as a supplementary storage device to batteries in hybrid vehicles to help extend the battery life [11]–[13]. In fuel-cell powered vehicles, ultracapacitors have been considered as an auxiliary power source which can assist the fuel cell during startup and fast power transients [14]–[17]. A concept BMW X3 which was unveiled in 2006, had an ultracapacitor-powered electric motor integrated between the combustion engine and the transmission, helping to augment the engine power when accelerating . From the perspective of energy management, powertrains with ultracapacitors present special challenges due to their low energy storage capacity and constraints on the state of charge becoming frequently active. For instance, the popular ECMS strategy [18] for HEVs is derived under idealized assumptions from the Pontryagin's maximum principle without consideration of state of charge constraints; as a result, such a policy may not be near optimal for ultracapacitor assisted powertrains.

In this paper, our objective is to assess the extent to which an ultracapacitor, as a standalone power assist device, can improve the fuel economy of a mid-size passenger vehicle without sacrificing the vehicle's ability to follow a given velocity profile. In a mild parallel hybrid configuration, an induction motor powered by an ultracapacitor module assists the combustion engine during acceleration power peaks, and is recharged back either by the engine during normal cruise, or through regenerative braking. The fuel economy of such a powertrain depends on choices of both powertrain parameters and energy management control strategy. Both choices will be examined in this paper. On the control side, a rule-based energy management strategy and a model predictive control (MPC) strategy will be designed and evaluated in simulations. The selection of hardware parameters and the final simulation assessment of the control algorithms will be performed on a higher fidelity model. A lower fidelity, yet much lower complexity model will be utilized in the control design.

II. Hybrid Powertrain Configuration and Models

A parallel hybrid configuration, shown in Fig. 2, was chosen in which the torques supplied by the engine and motor are additive. The configuration used in this study is known as a mild hybrid, because the engine has been sized large enough to meet the vehicle's peak power demands on its own, should the ultracapacitor be unable to assist [3]. This choice was made to account for the ultracapacitor's low energy density, which imposes a limit on the amount of assistance the motor can sustain between recharge cycles. For this study, the motor is placed before the transmission, and the rotational speeds of the engine and motor are assumed to be the same.[3]

[3]Different arrangements can be realized through the addition of torque coupling, not considered here.

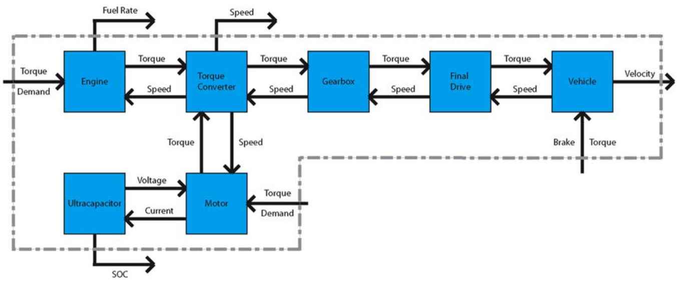

Fig. 3. Diagram showing the flow of information through the plant of the full-order model.

A two-wheel drive full-size SUV powertrain with a 6 cylinder, 4 liter, 160 kW engine was selected as the baseline for our study. With the help of Powertrain Systems Analysis Toolkit (PSAT) package [19], two models of the hybrid powertrain were created. These models are based on the PSAT model, but they operate independently from the PSAT software. The first model is a full-order model created for simulation of the powertrain under various driving conditions, and contains three primary states. The second is a single-state model which captures the ultracapacitor's state-of-charge dynamics for use in control design, and is referred to as the reduced-order model.

A. Full-Order Model

Fig. 3 shows the plant signal structure for the full-order model. This is a causal forward-looking model of the powertrain. The torque commands to the engine, motor, and brakes determined by the power management strategy are the inputs to the model. The fuel rate of the engine and the state of charge of the ultracapacitor are the main outputs of interest. The vehicle velocity, the torque converter input speed, and ultracapacitor state-of-charge are the primary dynamic states of the full-order model. The full-order model uses maps and parameters from the PSAT which were experimentally determined by Argonne National Laboratory and its industrial partners. However, the signal structure of the model has been changed, with more computations being handled at the component level, and some of the components themselves have been simplified. The controller used by PSAT has been replaced by strategies explained in Sections III and IV. For completeness, the main component models are described in this section. Two tables summarizing the variables and parameter values of the full-order model are provided in the Appendix.

1) Ultracapacitor Model: The open-circuit voltage of the ultracapacitor is given by

$$V_{\mathrm{uc,oc}} = \frac{q_{\mathrm{uc}}}{C_{\mathrm{uc}}} \tag{1}$$

where the capacitance C_{uc}, varies slightly with the ultracapacitor's internal temperature and current. This relationship is given by a map shown in Fig. 4. These and other component maps in this paper were obtained using empirical data taken from PSAT database [19]. The charge dynamics of the ultracapacitor are given by

$$\frac{dq_{\mathrm{uc}}}{dt} = -i_{\mathrm{uc}} \tag{2}$$

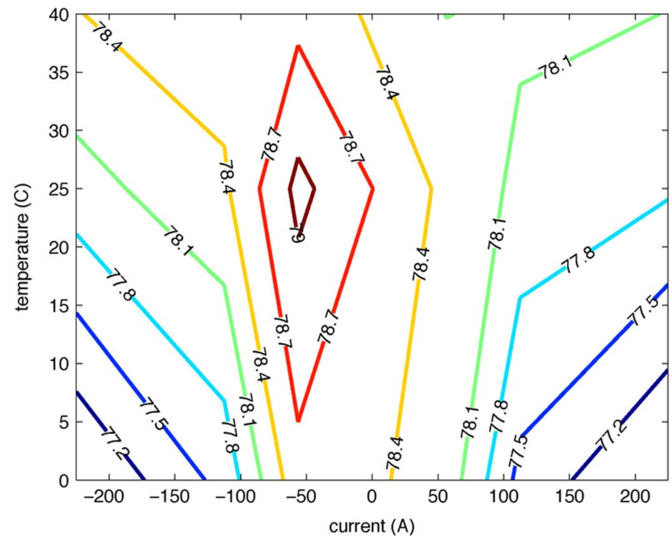

Fig. 4. Contour plot which shows the capacitance (in F) as a function of temperature and current.

where i_{uc} is the current being drawn. Positive and negative current correspond to discharging and charging, respectively. The state-of-charge is a normalized parameter representing the amount of charge remaining in the ultracapacitor, and is equal to

$$\mathrm{soc} = \frac{V_{\mathrm{oc,uc}} - V_{\mathrm{min,uc}}}{V_{\mathrm{max,uc}} - V_{\mathrm{min,uc}}} \tag{3}$$

where $V_{\mathrm{max,uc}}$ and $V_{\mathrm{min,uc}}$ are the maximum and minimum open-circuit voltages. The effective voltage provided by the ultracapacitor is

$$V_{\mathrm{out,uc}} = V_{\mathrm{oc,uc}} - i_{\mathrm{uc}} R_{\mathrm{uc}} \tag{4}$$

where R_{uc} is the line resistance and assumed to be the same during charge and discharge [4]. This resistance varies with temperature and current, as shown in Fig. 5. The current drawn from the ultracapacitor is determined from the power P_{uc} demanded by motor, using the simple relation

$$i_{\mathrm{uc}} = \frac{P_{\mathrm{uc}}}{V_{\mathrm{out,uc}}}. \tag{5}$$

This power is bounded by the line losses in the ultracapacitor. The maximum charging and discharging power the capacitor can support are given as

$$P_{\mathrm{max,dis}} = \frac{V_{\mathrm{oc,uc}}^2}{4R_{\mathrm{uc}}} \tag{6}$$

$$P_{\mathrm{max,chg}} = V_{\mathrm{oc,uc}} \frac{V_{\mathrm{oc,uc}} - V_{\mathrm{max,uc}}}{R_{\mathrm{uc}}}. \tag{7}$$

Because the capacitance and line resistance are dependent upon temperature, the thermal dynamics of the ultracapacitor are modeled. The generated heat is related to the power losses in the system and calculated differently for discharging $(i_{\mathrm{uc}} > 0)$ and charging $(i_{\mathrm{uc}} < 0)$ intervals

$$Q_{\mathrm{gen,uc}} = \begin{cases} i_{\mathrm{uc}}^2 R_{\mathrm{uc}}, & i_{\mathrm{uc}} > 0 \\ i_{\mathrm{uc}}^2 R_{\mathrm{uc}} - i_{\mathrm{uc}} V_{\mathrm{out,uc}} \times (1 - \eta_{\mathrm{uc}}), & i_{\mathrm{uc}} < 0. \end{cases} \tag{8}$$

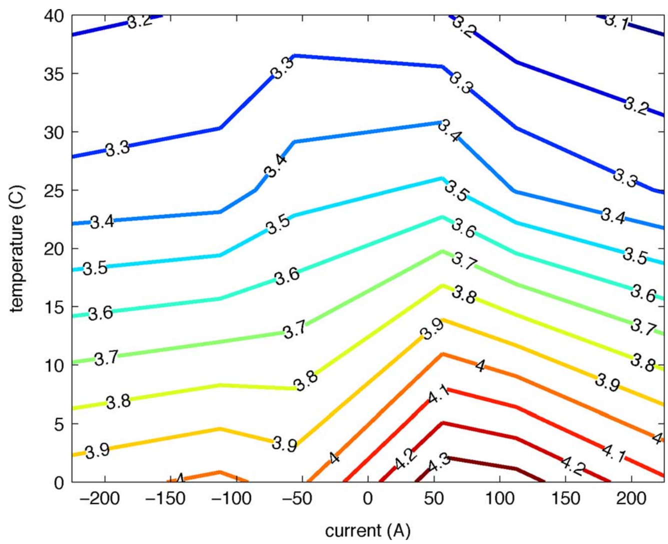

Fig. 5. Contour plot which shows the line resistance, in Ω and scaled by a factor of 100, as a function of temperature and current.

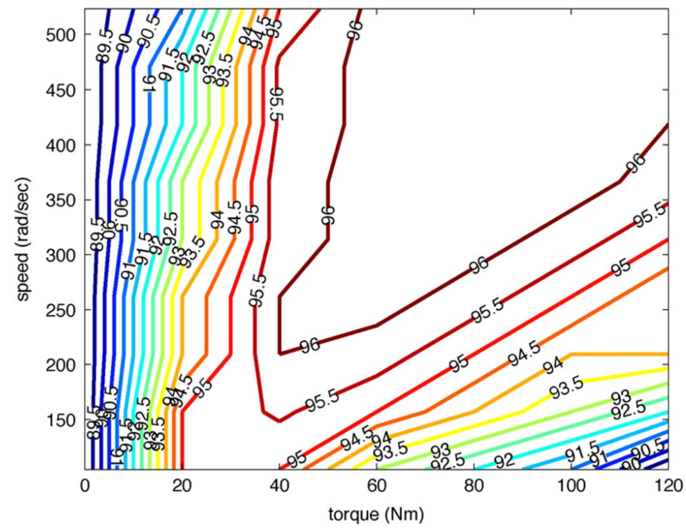

Fig. 6. Contour plot of the motor efficiency (in %) as a function of motor torque and speed.

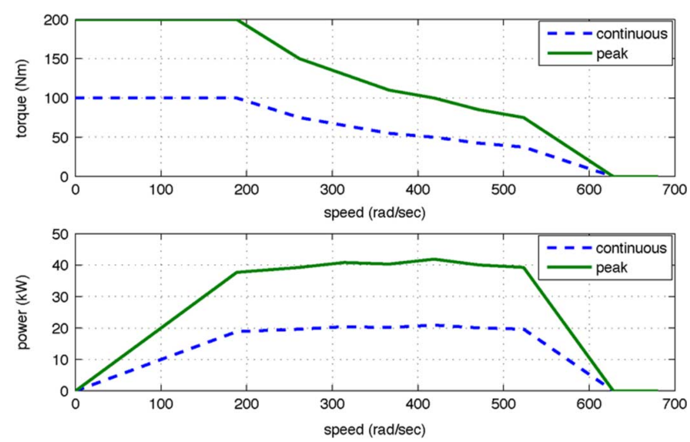

Fig. 7. Plot of peak and continuous torque and power of the motor, as functions of the shaft speed. The magnitudes represent both generating and propelling.

In this expression, η_{uc} is a charging efficiency of the ultracapacitor, separate from the line losses. The convective heat transfer between the case and the surrounding air is given by

$$Q_{\mathrm{case,uc}} = \frac{T_{\mathrm{air}} - T_{\mathrm{uc}}}{R_{\mathrm{therm,uc}}} \tag{9}$$

with $R_{\mathrm{therm,uc}}$ being the equivalent thermal resistance. T_{air} is the temperature of the air flowing across the surface, and is determined using terms from the previous time step

$$T_{\mathrm{air},t+\Delta t} = T_{\infty} - \frac{Q_{\mathrm{case,uc}}}{2\dot{M}_{\mathrm{air}} C_{p,\mathrm{air}}}. \tag{10}$$

$\dot{M}_{\mathrm{air}}$ and $C_{p,\mathrm{air}}$ are the mass flow rate and heat capacity of the air, and T_{∞} is the ambient temperature, assumed to be constant. Using these two heat flux sources, and the mass and heat capacity of the ultracapacitor, the temperature dynamics are expressed

$$M_{\mathrm{uc}} C_{p,\mathrm{uc}} \frac{dT_{\mathrm{uc}}}{dt} = Q_{\mathrm{gen,uc}} + Q_{\mathrm{case,uc}}. \tag{11}$$

2) Motor Model: The motor torque dynamics are much faster than those of the ultracapacitor, and the motor model does not have a dynamic state. The losses in the motor are dependent on both the shaft speed and the motor's output torque, and include the losses of the motor controller as well. The efficiency map corresponding to these losses is shown in Fig. 6. The electric power needed by the motor is mapped directly from the output torque and speed, with these losses taken into account

$$P_{\mathrm{uc}} = P_{\mathrm{map,mot}}(T_{\mathrm{mot}}, \omega_{\mathrm{mot}}). \tag{12}$$

The maximum electric power which can be supplied to the motor is limited by it's maximum allowable current, shown as

$$P_{\mathrm{max,mot}} = i_{\mathrm{max,mot}} V_{\mathrm{out,uc}}. \tag{13}$$

The maximum torque output of the motor is limited both electrically and mechanically. The mechanical torque limit is calculated by

$$\begin{aligned} T_{\mathrm{max,mech,mot}} &= T_{\mathrm{peak,mot}} \\ &\quad - \mathrm{HI} \times [T_{\mathrm{peak,mot}}(\omega_{\mathrm{mot}}) - T_{\mathrm{cont,mot}}(\omega_{\mathrm{mot}})]. \end{aligned} \tag{14}$$

$T_{\mathrm{cont,mot}}$ and $T_{\mathrm{peak,mot}}$ are the continuous and peak torques, which depend upon the current shaft speed, as shown in Fig. 7. The heat index, HI, adjusts the available torque between the peak and continuous torques during operation, and its dynamics are given by

$$\frac{d\mathrm{HI}}{dt} = \frac{0.3}{\tau_{\mathrm{max,mot}}} \left(\left| \frac{T_{\mathrm{mot}}}{T_{\mathrm{cont,mot}}} \right| - 1 \right) \tag{15}$$

where $\tau_{\mathrm{max,mot}}$ is a time constant of the motor. In general terms, the motor will be able to operate near the peak torque after resting, but will be forced towards the continuous torque limit during sustained operation. The output torque is also limited by

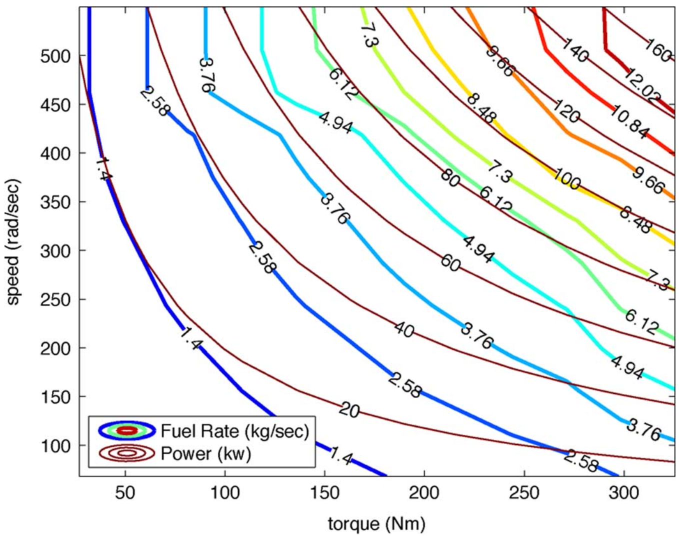

Fig. 8. Contour plot which shows the fuel consumption rate (in g/s) and power contours (in kW) of the engine as a function of engine torque and shaft speed.

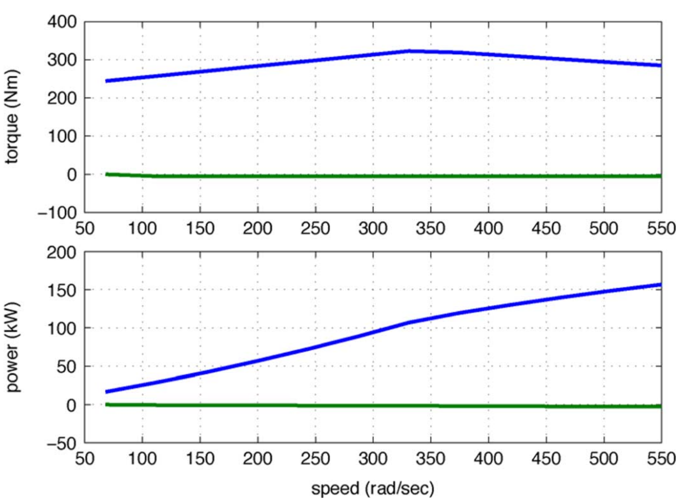

Fig. 9. Plot of the maximum and minimum indicated torques and powers generated by the engine. The lower boundary refers to the case in which no fuel is consumed.

the electrical power available to the motor, and this constraint is shown as

$$T_{\mathrm{max,elec,mot}} = P^{-1}_{\mathrm{map,mot}}(P_{\mathrm{max,mot}}, \omega_{\mathrm{mot}}) \tag{16}$$

where $P^{-1}_{\mathrm{map,mot}}$ denotes an inverse of the map used earlier, calculating torque from inputs of shaft speed and electric power. The maximum torque, $T_{\mathrm{max,mot}}$, that the motor can provide at any given moment, will be the more restrictive of the mechanical or electrical limitations.

3) Engine Model: The engine torque dynamics are modeled quasi-statically so that the *fuel consumption rate* of the engine is determined from engine torque and speed, using a static map obtained from the PSAT empirical data. A contour plot of this map is shown in Fig. 8. The constraints on engine indicated torque and power are empirically mapped from the engine speed shown in Fig. 9. The frictional losses of the engine are assumed to be constant, and are modeled by the term $P_{\mathrm{loss,eng}}$. The net engine output torque is thus defined as

$$T_{\mathrm{eng,out}} = T_{\mathrm{eng}} - \frac{P_{\mathrm{loss,eng}}}{\omega_{\mathrm{eng}}} \tag{17}$$

where T_{eng} is the engine indicated torque. During engine idling a constant fuel rate is assumed. A constant value for $P_{\mathrm{loss,eng}}$, reflective of average combined engine friction and accessory power losses over UDDS drive cycle, as observed in PSAT model, was assumed.

4) Torque Converter Model: In the proposed configuration, both the engine and the motor are directly linked to the torque converter. Therefore, the torques supplied by the engine and motor are additive, and the same rotational speed is shared between them

$$\begin{aligned} T_{\mathrm{in,tc}} &= T_{\mathrm{mot}} + T_{\mathrm{eng,out}} \\ \omega_{\mathrm{mot}} &= \omega_{\mathrm{eng}} = \omega_{\mathrm{in,tc}}. \end{aligned} \tag{18}$$

The rotational dynamics of the torque converter are characterized by

$$J\frac{d\omega_{\mathrm{in,tc}}}{dt} = T_{1,\mathrm{tc}} - T_{\mathrm{loss,tc}} \tag{19}$$

where J is the rotational inertia upstream of the torque converter, $\omega_{\mathrm{in,tc}}$ is the torque converter's input speed, and $T_{1,\mathrm{tc}}$ is the torque at the impeller of the torque converter. The loss in the torque converter, $T_{\mathrm{loss,tc}}$, is mapped as a function of $T_{\mathrm{in,tc}}, \omega_{\mathrm{in,tc}}$, and the slip ratio ω_{ratio}, defined as

$$\omega_{\mathrm{ratio}} = \frac{\omega_{\mathrm{out,tc}}}{\omega_{\mathrm{in,tc}}} \tag{20}$$

where $\omega_{\mathrm{out,tc}}$ is the rotational velocity of the powertrain downstream of the torque converter. The impeller torque $T_{1,\mathrm{tc}}$ is determined differently depending on the torque converter's operation mode. The torque converter is considered to be in "idle" mode when the rotational speed upstream $\omega_{\mathrm{in,tc}}$ is near the idling speed of the engine $\omega_{\mathrm{idle,eng}}$, that is when $0 \le \omega_{\mathrm{in,tc}} - \omega_{\mathrm{idle,eng}} \le 25$. In this mode, the torque converter behavior is expressed by

$$T_{1,\mathrm{tc}} = T_{\mathrm{in,tc}} - T_{2,\mathrm{tc}} \tag{21}$$

where $T_{2,\mathrm{tc}}$ is the torque at the turbine of the torque converter and is determined by

$$T_{2,\mathrm{tc}} = T_{\mathrm{in,tc}} \times \frac{\omega_{\mathrm{in,tc}} - \omega_{\mathrm{idle,eng}}}{100} \tag{22}$$

when $T_{\mathrm{in,tc}} > 0$ otherwise, $T_{2,\mathrm{tc}}$ is set to zero.

The second representative mode is the "quasi-static" mode. The torque converter is considered to be in this mode when operating near steady state and the conditions for idle mode are not met

$$T_{1,\mathrm{tc}} = T_{\mathrm{ratio}}(\omega_{\mathrm{ratio}})\frac{\omega_{\mathrm{in,tc}}|\omega_{\mathrm{in,tc}}|}{K^2(\omega_{\mathrm{ratio}})} \tag{23}$$

$$T_{2,\mathrm{tc}} = T_{\mathrm{in,tc}} - \frac{T_{1,\mathrm{tc}}}{T_{\mathrm{ratio}}(\omega_{\mathrm{ratio}})}. \tag{24}$$

Here, T_{ratio} is the torque ratio, and K is called the "capacity factor". Both parameters are mapped functions of the slip ratio ω_{ratio}. When the conditions for neither of the above two operating modes are met, the torque converter is considered to be in "transient" mode, and its behavior is described by

$$T_{1,\text{tc}} = |T_{\text{in,tc}}|\frac{\omega_{\text{goal}} - \omega_{\text{in,tc}}}{25} - 0.01|T_{\text{in,tc}}| \leq T_{1,tc} \leq 0.75|T_{\text{in,tc}}| \tag{25}$$

$$T_{2,\text{tc}} = (T_{\text{in,tc}} - T_{1,\text{tc}}) \times T_{\text{ratio}}(\omega_{\text{ratio}}) \tag{26}$$

where ω_{goal} is an intermediate variable described by

$$\omega_{\text{goal}} = \sqrt{|T_{\text{in,tc}}|} \times K(\omega_{\text{ratio}})$$
$$\omega_{\text{idle,eng}} + 20 \leq \omega_{\text{goal}} \leq 310. \tag{27}$$

The torque ouput of the torque converter $T_{\text{out,tc}}$ is equal to its turbine torque $T_{2,\text{tc}}$.

5) Gearbox Model: The gearbox is modeled as a gear ratio and a loss term. The torque supplied by the gearbox to the driveline is given by

$$T_{\text{out,gb}} = G_t \times (T_{\text{out,tc}} - T_{\text{loss,gb}}) \tag{28}$$

where $T_{\text{loss,gb}}$ is mapped as

$$T_{\text{loss,gb}} = T_{\text{loss,gb}}(\omega_{\text{out,gb}}, T_{\text{out,tc}}, G_t) \tag{29}$$

where the output speed is

$$\omega_{\text{out,gb}} = \frac{\omega_{\text{in,gb}}}{G_t}. \tag{30}$$

Immediately after a gear shift, the input speed is passed through a first-order filter, to prevent numerical problems due to large instantaneous changes in speed

$$0.2\dot{\omega}_{\text{in,gb,filtered}} + \omega_{\text{in,gb,filtered}} = \omega_{\text{in,gb}}. \tag{31}$$

The gear ratio, G_t, is determined by the same shifting strategy that PSAT uses in its simulations. The optimization of shifting schedule represents an additional opportunity [20] to affect fuel economy improvements. The shifting strategy optimization will be explored in future work.

The wheel torque and gearbox speed are also influenced by the final drive ratio

$$T_w = g_f \times T_{\text{out,gb}} - T_{\text{loss,fd}} \tag{32}$$
$$\omega_{\text{out,gb}} = \omega_w \times g_f \tag{33}$$

where the final drive ratio g_f, and the loss term $T_{\text{loss,fd}}$, are constants.

6) Vehicle Longitudinal Dynamics: The vehicle longitudinal dynamics are

$$M\frac{dv}{dt} = \frac{T_w}{r_w} - F_{\text{grade}} - F_{\text{drag}} - F_{\text{brake}} \tag{34}$$

where M and v are the mass and velocity of the vehicle, r_w is the wheel radius, and F_{grade} is the force due to weight and road grade, calculated as

$$F_{\text{grade}} = [\sin(\theta) + (\mu_1 + \mu_2\omega_w)\cos(\theta)]\text{Mg} \tag{35}$$

where μ_1 and μ_2 are friction coefficients [21], and θ is the road grade. The aerodynamic drag force is

$$F_{\text{drag}} = Cv^2 \tag{36}$$

where C is a scaled drag coefficient [21]. Assuming no wheel slip, the rotational speed of the axle is calculated from the vehicle velocity by

$$\omega_w = \frac{v}{r_w}. \tag{37}$$

The friction brake force at the wheels is represented by F_{brake}. The friction brakes themselves are not modeled, and it is assumed that the they can provide any demand that the cycle will require of them.

B. Reduced-Order Model

The details incorporated into the full-order model make it a reliable tool for simulation, but they also make it too complex for use in model-based control design. In order to simplify the control design process, a reduced-order model of the powertrain is developed, containing the ultracapacitor state-of-charge as its only state. This model is simplified to a backward-looking model, as opposed to the causal and forward-looking full-order model. The torque converter, transmission, and the vehicle longitudinal dynamics are external to the reduced-order model, and the full-order model is used to calculate the engine and motor speeds, as well as the torque demand upstream of the torque converter. Because the controller only determines the power split ratio between the engine and the motor, it uses the torque demand and speed upstream of the torque converter as inputs. Backward-looking modeling facilitates this approach. Fig. 10 shows the signal flow in the reduced-order model. The state-of-charge is described by

$$\frac{d\text{soc}}{dt} = -\frac{i_{\text{uc}}}{CV_{\max}} = \frac{-\text{soc}V_{\max} + \sqrt{(\text{soc}V_{\max})^2 - \frac{4RP_{\text{mot}}}{\beta}}}{2RCV_{\max}}. \tag{38}$$

The coefficient β, is

$$\beta = \begin{cases} \eta_{\text{mot}}, & \text{while discharging} \\ 1/\eta_{\text{mot}}, & \text{while charging} \end{cases} \tag{39}$$

where η_{mot} represents the motor efficiency. In the reduced-order model, it is assumed that the line resistance R and capacitance C are independent of internal temperature of the ultracapacitor and are constant. The full derivation for (38) can be found in [22]. In a related work [23], we have found that the model (38) is sufficiently accurate to be used for experimental controller

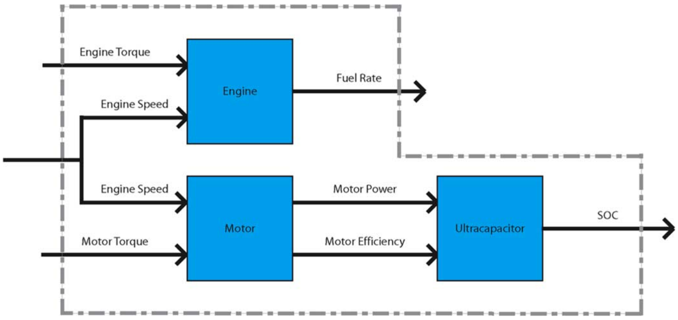

Fig. 10. Diagram showing the flow of information through the plant of the reduced-order model. Inputs are the torque demands and shaft speed of the motor and engine. Outputs are the rate of fuel consumption and the state-of-charge.

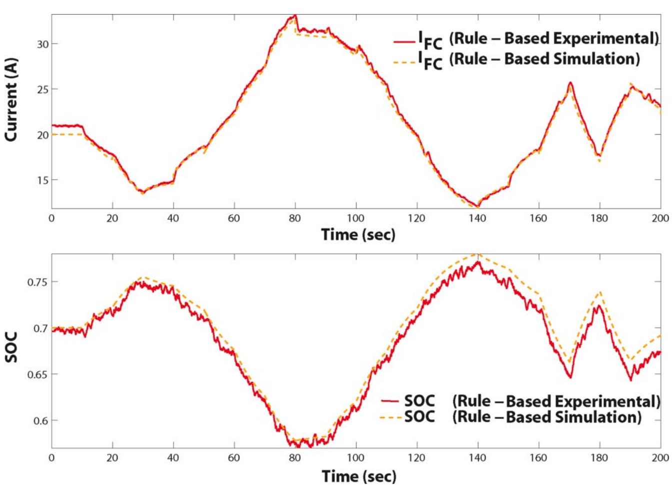

Fig. 11. Ultracapacitor model verified experimentally in [23]. The second subplot shows the ultracapacitor state of charge variation in a fuel cell-ultracapacitor hybrid setup.

development. Fig. 11 shows that simulation results produced with (38) matched our experimental results.

In the reduced-order model the engine fuel consumption rate and motor efficiencies are modeled algebraically, using the Willan's line method

$$\dot{m}_f = \frac{aT_{\text{eng}}\omega_{\text{eng}} + b\omega_{\text{eng}} + c\omega_{\text{eng}}^3}{\bar{a} + \bar{b}\omega_{\text{eng}} + \bar{c}\omega_{\text{eng}}^2} \tag{40}$$

$$\eta_{\text{mot}} = \frac{e_{\text{mot}}T_{\text{mot}}\omega_{\text{mot}}}{T_{\text{mot}}\omega_{\text{mot}} + P_{\text{loss,mot}}} \tag{41}$$

where $\omega_{\text{eng}}, \omega_{\text{mot}}, T_{\text{eng}}$, and T_{mot} are the rotational velocities and output torques of the motor and engine, respectively. η_{mot} is the energy efficiency of the motor, and $\dot{m}_f$ is the mass consumption rate of fuel. The other parameters ($e_{\text{mot}}, P_{\text{loss,mot}}, a, b, c, \bar{a}, \bar{b}$, and $\bar{c}$) are determined numerically from the characteristic maps of the selected engine and motor available in the PSAT database. While Fig. 11 shows good match between experimental measurements and reduced order model prediction in terms of ultracapacitor charging, other aspects of the model are crude compared to the full order model. In particular, the inferred from vehicle speed trajectory torque demand and speed upstream of the torque converter (inputs of the reduced order model) are considerably more aggressive than in the forward looking full order model, perhaps corresponding to those of an aggressive driver. For this reason, the reduced order model overestimates fuel consumption as compared to the full order model, but is still appropriate for directional studies.

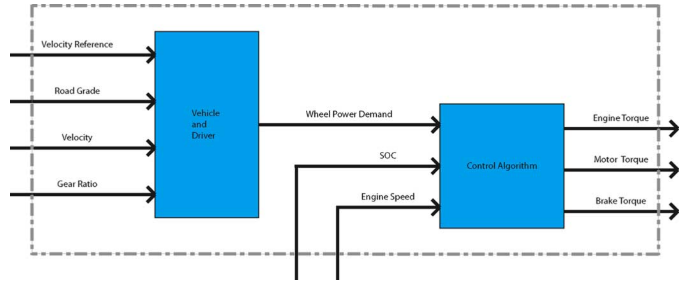

Fig. 12. Overview of the signal structure of the rule-based controller.

In this paper, a full spectrum of power management strategies is explored. A simple rule-based strategy for power management is presented first. Simplicity and expedience in both tuning and implementation make this method useful for testing the impact of different component combinations on fuel economy. With a suitable combination of engine, motor, and ultracapacitor sizes having been determined through simulation, later sections focus on the use of optimal control techniques. Dynamic programming is used to present an estimate of the best possible fuel economy, and then the design process for a model predictive control strategy is presented and implemented. The performance of this control strategy is then compared with those of the rule-based strategy and the dynamic programming results.

III. Rule-Based Power Management

The rule-based power management algorithm receives the total power demand at the wheels as an input and determines the power split between the engine, the motor, and the friction brakes. The wheel power demand is calculated by a vehicle and driver model, shown in Fig. 12. This model uses the velocity, reference velocity, and road grade to calculate the power demanded at the wheels, and is based on the longitudinal dynamics of the full-order model. The driver is modeled as a simple proportional controller and calculates a desired acceleration proportional to the difference between the vehicle velocity v, and the predetermined cycle velocity v_{ref}

$$\dot{v}_{\text{dem}} = K_{\text{driver}}(v_{\text{ref}} - v). \tag{42}$$

The torque demand at the wheels is a function of this desired acceleration and the forces due to drag and road grade

$$T_{\text{dem}} = [\dot{v}_{\text{dem}}(J + Mr_w) + [F_{\text{grade}} + F_{\text{drag}}]r_w] \tag{43}$$

where the terms F_{grade} and F_{drag} are the same as those shown in (36) and (35). The constant J represents the rotational inertia of the powertrain, and is given by

$$J = J_w + G_t^2(J_{\text{eng}} + J_{\text{mot}}) \tag{44}$$

where J_w, J_{eng}, and J_{mot} are the rotational inertias of the motor, engine, and wheels, respectively. Using the provided rotational velocity of the wheels, the required torque calculated in (43)

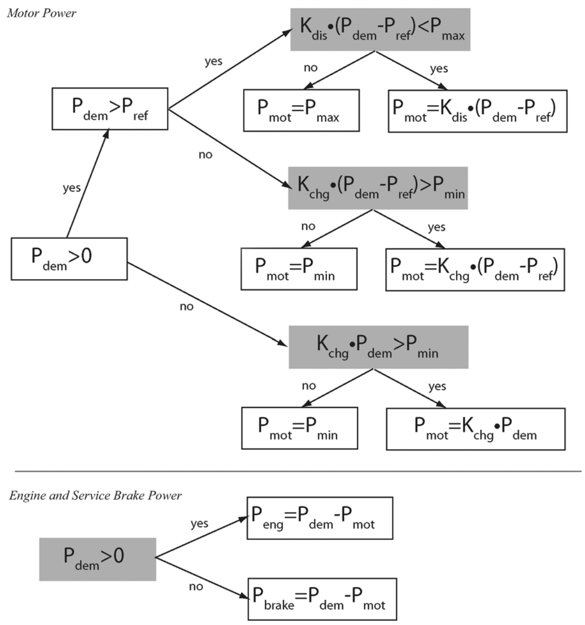

Fig. 13. Flow chart showing the decision tree of the rule-based control algorithm.

TABLE I
DIFFERENT MOTOR SIZES TESTED

Max. Power (kW)	Continuous Power (kW)	Weight (Kg)
40	21	30
70	35	115
110	75	92

TABLE II
DIFFERENT ULTRACAPACITOR SIZES TESTED

Voltage (V)	Cap (F)	Energy (Wh)	Weight (Kg)
93	78	93.7	35.46
93	156	187.4	70.92
93	234	281.1	106.38

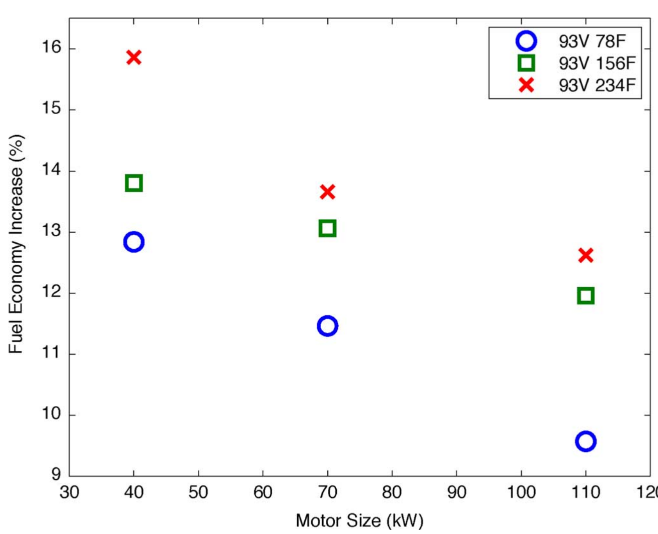

Fig. 14. Percent increase in fuel economy between conventional powertrain and hybrid powertrain with various motor and ultracapacitor sizes, applied over the UDDS driving cycle with 160 kW engine.

is converted into the power demand for the rule-based control algorithm

$$P_{\text{dem}} = \omega_w T_{\text{dem}}. \tag{45}$$

The power-split decision tree of the rule-based control algorithm is shown in Fig. 13. During propulsion ($P_{\text{dem}} > 0$), the rule-based algorithm commands the motor to assist the engine when the power demand is greater than a threshold P_{ref}, and commands the engine to charge the motor when the demand is less than P_{ref}. The value of P_{ref} is a function of engine speed, and is obtained from the engine's most efficient power curve, adjusted down by a gain.[4] It is this gain which provides the actual tuning parameter for the controller, and the reliance on this single degree of freedom which allows the rule-based strategy to be tuned quickly. During braking ($P_{\text{dem}} < 0$), the motor charges the ultracapacitor. Friction brakes are assumed to be engaged anytime the braking power falls outside of the motor's lower power limit $P_{\min}$. The motor is also restricted from charging the ultracapacitor while the engine speed is below the idling speed. During both propulsion and braking the controller also enforces upper and lower state-of-charge boundaries of $\text{soc}_{\max} = 0.9$ and $\text{soc}_{\min} = 0.5$, respectively. The imposed upper bound of 0.9 prevents against overcharging. The lower bound of 0.5 is chosen for efficiency of operation, because the primary power loss in the ultracapacitor is proportional to the square of the current (4), and a lower state-of-charge results in a lower output voltage (3), requiring a higher current to be drawn for a given power demand (5). The magnitude of the motor's power demand in either direction (generating or propelling) is scaled by the distance of the state-of-charge from its enforced boundaries, according to

$$K_{\text{chg}} = \frac{\text{soc}_{\max} - \text{soc}}{\text{soc}_{\max} - \text{soc}_{\min}} \tag{46}$$

$$K_{\text{dis}} = \frac{\text{soc} - \text{soc}_{\min}}{\text{soc}_{\max} - \text{soc}_{\min}}. \tag{47}$$

This scaling keeps the motor demand from changing abruptly when one of the state-of-charge boundaries is reached.

A. *Component Sizing*

The fuel economy gain with different sizes of motor, ultracapacitor, and engine was evaluated with the *full-order model* and rule-based controller. Induction motors with maximum power of 110, 70, and 40 kW were combined with 160 and 120 kW engines and three sizes of ultracapacitors. Tables I and II summarize the components used.

The fuel economy of each case was compared to that of the conventional vehicle with a 160 kW engine in full-order model simulations. The fuel economy of the conventional vehicle over the UDDS cycle was found to be 19.4 miles per gallon. Figs. 14 and 15 summarize the fuel economy improvement for UDDS cycle tests, with the 160 and 120 kW engines, respectively. The hybrid powertrains were able to produce the results shown while still following the cycle velocity. Comparative velocity plots are not shown, because the velocity profiles are indistinguishable from those of the conventional case. As seen in these figures, the smaller 40 kW motor gives the best fuel economy results of

[4]In a hybrid-drive running the engine at its standalone most efficient region is not equivalent to running the whole system more efficiently.

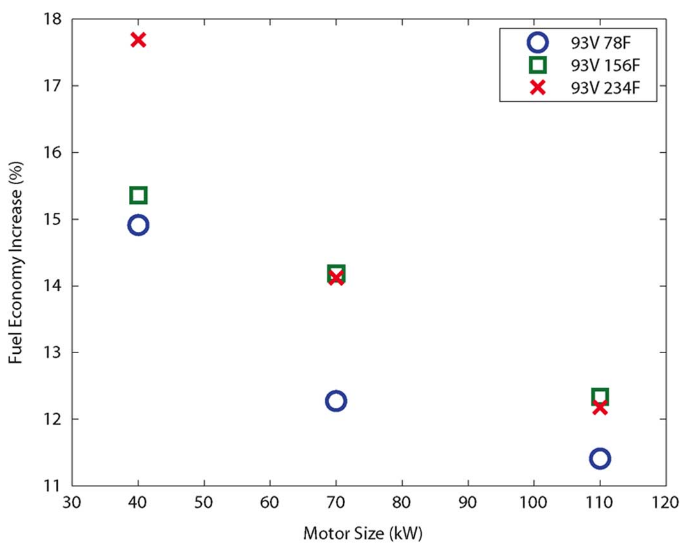

Fig. 15. Percent increase in fuel economy between conventional powertrain and hybrid powertrain with various motor and ultracapacitor sizes, applied over the UDDS driving cycle with 120 kW engine.

the three, and in light of this information, the 40 kW motor was chosen for future simulations.

The larger ultracapacitor modules result in better fuel economy, however we show in [24] that this may not be generalized to uphill grades. Higher weight of larger capacitors may offset their benefits on steep hills. Moreover the larger sizes (> 100 Wh) may not be an economically viable alternative to batteries according to [3]. Therefore, the 93 V 78 F ultracapacitors is chosen for the rest of simulations in this paper.

Comparing Figs. 14 and 15 shows that the smaller 120 kW engine achieves a better fuel economy for most combinations of motor and ultracapacitor size. However, due to the limited overall energy stored in the ultracapacitor, it may be very difficult to ensure that the motor will always have an energy supply to assist with during power spikes. In fact the vehicle with 120 kW engine alone was not able to meet the power demands of the UDDS cycle when run on a 5% grade or when ran on New York city cycle without loss of drivability. Because of this, it may not be viable to size the engine below that which could meet the driver's power demands on its own. Therefore, the 160 kW engine is chosen for the rest of the simulations in this paper.

Shown in Figs. 16–18 is a time history of several of the performance characteristics of the powertrain over the UDDS cycle with no road grade, using the selected 160 kW engine, 40 kW electric motor, and the 93 V 78 F ultracapacitor modules. Looking at Fig. 16, notice that the motor's assistance is rarely much higher than 15 kW, which helps to explain the inferior performance of the larger motors tested earlier. This simulation showed a fuel economy improvement of slightly more than 12.8% over the conventional powertrain. The results also indicate that the energy provided by regenerative braking is more than sufficient to sustain the motor's assistance to propulsion for these driving conditions, and that the motor is only utilizing a portion of the available braking energy.

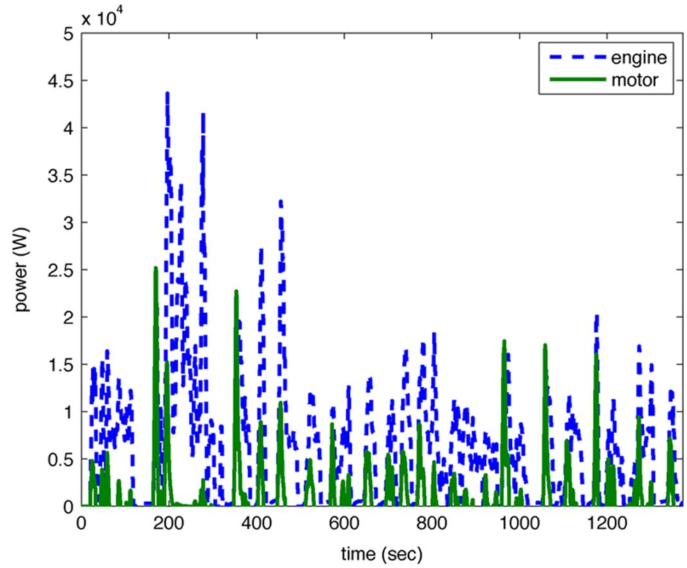

Fig. 16. Time history of power provided by the motor and the engine during propulsion of the vehicle over UDDS cycle with zero percent road grade, using a 160 kW engine and 40 kW motor.

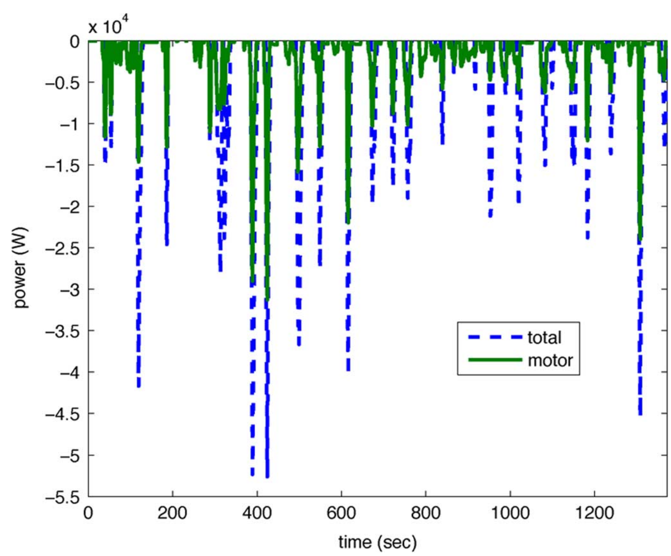

Fig. 17. Time history of power provided by the motor and the friction brakes during braking of the vehicle over UDDS cycle with zero percent road grade, using a 160 kW engine and 40 kW motor.

IV. Optimization-Based Supervisory Control

While a rule-based scheme can be perfected by excessive tuning and reliance on statically optimized-maps, its optimality cannot be guaranteed for every driving condition. The reason is large variations of vehicle operating conditions from one driving cycle to another, and the limitations of a rule-based control scheme by the structure of its rules. If instead, the vehicle's power management is formulated as a dynamic optimization problem, the fuel economy potential of the hybrid at its best may be determined. This is challenging however, as such optimization problems are typically highly nonlinear and subject to several dynamic constrains of the engine, motor, energy storage, and vehicle. Though analytical solutions to power

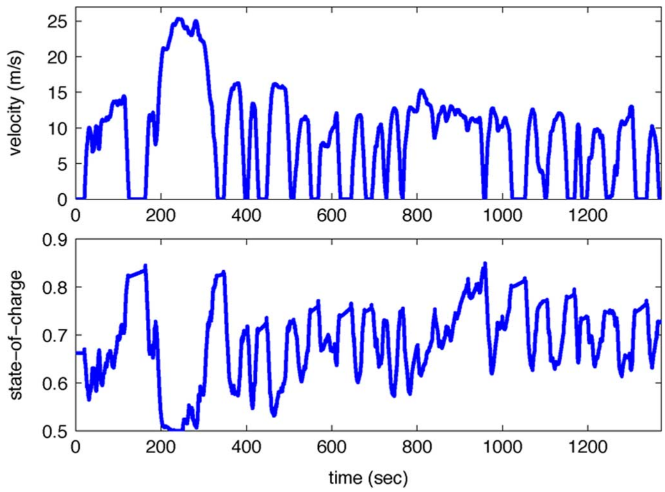

Fig. 18. Time history of vehicle velocity and ultracapacitor state-of-charge over UDDS cycle with zero percent road grade, using a 160 kW engine and 40 kW motor.

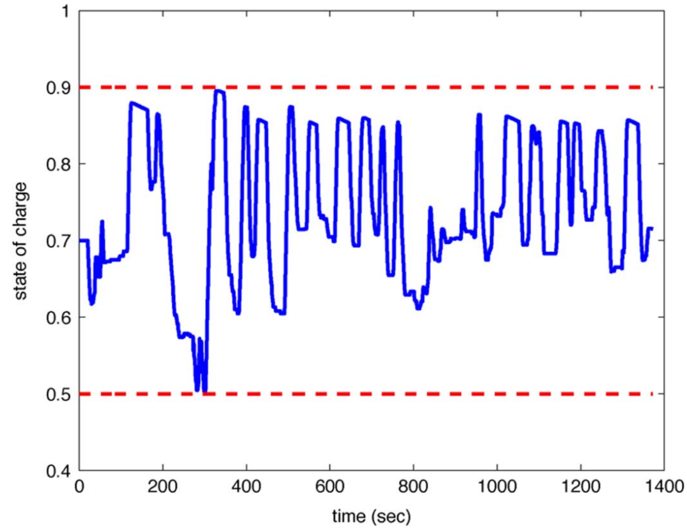

Fig. 19. Trajectory of the ultracapacitor state-of-charge when $P_{\rm mot}$ is optimally controlled, applied over the UDDS driving cycle with no road grade. Pointwise-in-time constraints on soc are shown by the dashed lines.

management do not exist in general, attempts have been made to cast and solve these problems in a standard optimal control framework [25]–[27]. The primary obstacle to this approach is a lack of information about upcoming driving conditions. Numerical solutions to the optimal control problem are the most widely used and among these is the Dynamic Programming (DP), see, e.g., [28] and references therein. Assuming known future driving conditions, DP can find the power management policy which results in the best fuel economy for a given driving cycle. In this section, the fuel economy potential of the ultracapacitor hybrid is first determined by DP applied over the UDDS driving cycle. Since DP is non-causal and not directly implementable in real-time, the optimization is then cased in a MPC framework, which is expected to produce near-optimal solutions in a causal manner. An MPC optimization problem can be converted to a quadratic program (QP), which can be efficiently solved online in polynomial-time.

The full-order model is too complex for use in DP and MPC design, because it contains many lookup tables, logical switches, and several dynamic states. These complexities would result in prohibitively large optimization computations for DP and complicate a linear MPC design. With the full-order model being too complex to be practical, the reduced-order model is used instead, having been created with this purpose in mind. Once the merit of the proposed optimization-based methods is established using the reduced-order model, the MPC strategy will be applied to the full-order plant model in simulations.

A. Dynamic Programming

The fuel economy potential of the ultracapacitor hybrid powertrain was first estimated using deterministic dynamic programming (DDP). Computationally, DDP reduces to value function iterations of the form

$$V(x,t) = \min_{u}\{L(x,u,w(t)) + V(f(x,u,w(t)),t+1)\} \tag{48}$$

where, assuming the reduced order model, t is the time instant over the drive cycle (sampling interval of 100 ms was used), x is the state (soc), u is the control ($u = s_f, P_{\rm mot} = s_f \cdot P_w$ and s_f is referred to as the split fraction), $w(t)$ is the vector of vehicle speed and vehicle power prescribed by the drive cycle, L is the incremental cost function, and the optimal control sequence, $\{u(t)\}$, is a minimizer in (48). The incremental cost L was chosen as a weighted sum of the fuel flow rate. Constraints on state of charge, soc, (specifically, $0.5 \leq {\rm soc}(t) \leq 0.9$ and that soc at the end of the drive cycle must be between 0.7 and 0.75) were imposed by augmenting to L, appropriate penalty functions (as per approach in [29]). The control constraints have been defined so that the expression under the square root in (38) is non-negative, thereby guaranteeing that the motor power $P_{\rm mot}$ can be realized by the ultracapacitor, and that $-1 \leq s_f \leq 1$ if $P_w \geq 0$ and $0 \leq s_f \leq 1$ if $P_w < 0$. Further a vehicle velocity dependent constraint on minimum and maximum motor power limits has been imposed.

DDP was applied to the *reduced-order* model of the powertrain equipped with the 160 kW engine and 40 kW motor. The system was subjected to a power demand history corresponding to the UDDS driving cycle with no road grade. Figs. 19 and 20 illustrate the trajectory of soc and the difference in the fuel flow rate between the case when $P_{\rm mot} = 0$ and when $P_{\rm mot}$ is optimally controlled. The fuel consumption difference between these two cases is 11.9% and it provides an estimate for achievable performance when optimization of control as a function of time is performed against a drive cycle known in advance. Fig. 19 shows that the constraints on the state of charge are satisfied. When the rule-based controller was applied to the reduced-order plant model, it was able to only achieve a fuel economy improvement of 5.0% over the $P_{\rm mot} = 0$ case, a mere fraction of the estimated improvement potential of 11.9%. This fuel economy gain through optimization motivates the next step in developing the optimization-based model predictive control scheme which unlike the DDP approach is causal.

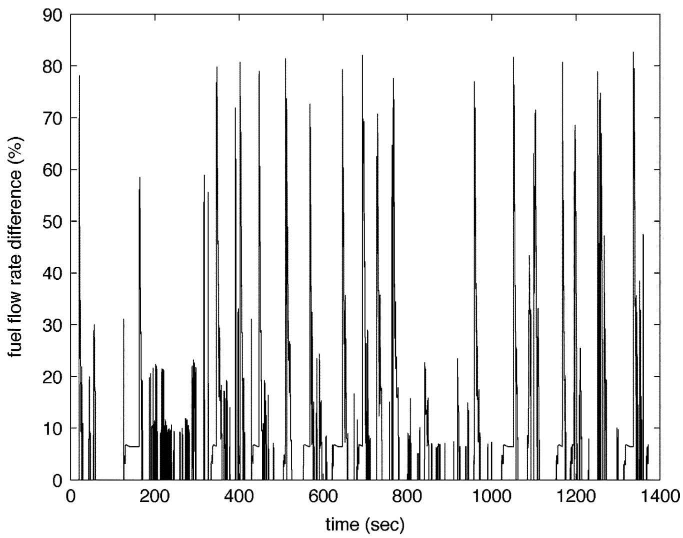

Fig. 20. Percent difference in fuel flow rate between the case when $P_{\rm mot} = 0$ and when $P_{\rm mot}$ is optimally controlled, applied over the UDDS cycle with no road grade.

B. MPC

The *reduced-order* plant model is used for design of the MPC strategy. The state, control input, measured disturbance, and the output vectors are respectively

$$x = [\mathrm{soc}], \quad u = [T_{\rm eng}],$$
$$w = [T_d \quad \omega_d]^T, \quad y = [\mathrm{soc} \quad \dot{m}_f]^T.$$

Here the engine torque $T_{\rm eng}$ is chosen as the control input. The measured disturbances T_d and ω_d are the torque demand and shaft speed upstream of the torque converter respectively and are imposed by the driving cycle and a backward model of the transmission. The motor torque is simply obtained from $T_{\rm mot} = T_d - T_{\rm eng}$; the engine and motor speeds are equal to ω_d [see (18)]. The reduced-order plant model is linearized around a representative operating point which corresponds to a region in which the motor and engine are propelling, and the ultracapacitor is discharging. The result can be expressed as the following single-state linear state-space system:

$$\begin{aligned} \dot{x} &= Ax + B_u u + B_w w + d \\ y &= Cx + D_u u + D_w w \end{aligned} \tag{49}$$

where A, B_u, B_w, C, D_u, and D_w are the linearized system matrices and the term d is a constant that reflects the difference between the nonlinear system and its linearized version at the operating point

$$d = f(x_o, u_o, w_o) - Ax_o - B_u u_o - B_w w_o.$$

Here x_o, u_o, w_o, and y_o denote the operating point values of state, control input, measured disturbance, and the output, respectively. The term $f(x_o, u_o, w_o)$ is the right-hand side of (38) evaluated at the chosen operating point. Note that except for when $P_{\rm mot} = 0$, the operating point will not be an equilibrium of the system and therefore $f(x_o, u_o, w_o)$ is nonzero in general. The term d is treated as a constant measured disturbance.

In the proposed MPC approach the energy management problem is cast as a moving horizon optimization problem. This is different from DP for which the optimization horizon included the whole cycle and the cycle was assumed known in advance. The MPC design objective is to minimize the total fuel consumption while also respecting the pointwise-in-time constraints on engine torque, motor torque, and state-of-charge. With this in mind, a finite-horizon quadratic cost function is formed which penalizes fuel use $\dot{m}_f$, deviation of state-of-charge from a reference value $\mathrm{soc}_{\rm ref}$, and also penalizes excessive use of engine torque $T_{\rm eng}$. At the kth sample time t_k the cost function is

$$J(t_k) = \sum_{t=t_k}^{t_{k+P}} q_1\|\mathrm{soc}_{\rm ref} - \mathrm{soc}(t)\|^2 + q_2\|\dot{m}_f(t)\|^2 + q_3\|T_{\rm eng}(t)\|^2 \tag{50}$$

where $t_{k+1} = t_k + \Delta t$, and Δt is a fixed sampling time. P is the prediction horizon, and the scalars q_i, represent the penalty weights. These weights can be adjusted, along with $\mathrm{soc}_{\rm ref}$, to shape the performance of the MPC power management scheme. The upper and lower bounds on ultracapacitor state-of-charge, motor torque limits (see Fig. 7), and engine torque limits (see Fig. 9) should also be enforced as (time-varying) inequality constraints $\forall t \in \{t_k, t_{k+1}, \ldots, t_{k+P}\}$

$$\begin{aligned} 0 \le T_{\rm eng}(t) &\le T_{\rm max,eng}(\omega_{\rm eng}(t)) \\ -T_{\rm max,mot}(\omega_{\rm mot}(t)) \le T_{\rm mot}(t) &\le T_{\rm max,mot}(\omega_{\rm mot}(t)) \\ 0.5 \le \mathrm{soc}(t) &\le 0.9. \end{aligned} \tag{51}$$

The cost function (50) is minimized at each sample time subject to the model (49) discretized[5] with sampling period Δt, and the inequality constraints in (51). This determines the sequence of next $N \leqslant P$ control inputs $U(t_k) = [T_{\rm eng}(t_k) \quad T_{\rm eng}(t_{k+1}) \quad \cdots T_{\rm eng}(t_{k+N-1})]$ over the future horizon P. When $N < P$ the remaining control moves $[T_{\rm eng}(t_k) \quad T_{\rm eng}(t_{k+1}) \quad \cdots T_{\rm eng}(t_{k+N-1})]$ are assumed to be zero. According to the standard MPC design, only the first element of the control sequence $U(t_k)$ is applied to the vehicle, the optimization horizon is moved one step forward, the model and constraints are updated if necessary, and the optimization process is repeated to obtain the next optimal control sequence $U(t_{k+1})$ (see [30] and [31] for more details of MPC design). A schematic of the MPC block is shown in Fig. 21.

In simulated implementation, the MPC power management scheme is tested on both reduced- and full-order nonlinear models of the plant. The MPC controller is used only in propulsion mode (positive power demand). During braking (negative power demand) no optimization is necessary; regenerative braking should be given first priority as long as the motor and ultracapacitor charge limits allow, and beyond this the service

[5]The direct injection of inputs in the output equation is removed by augmenting auxiliary states with fast dynamics to the system. Details are standard and omitted here.

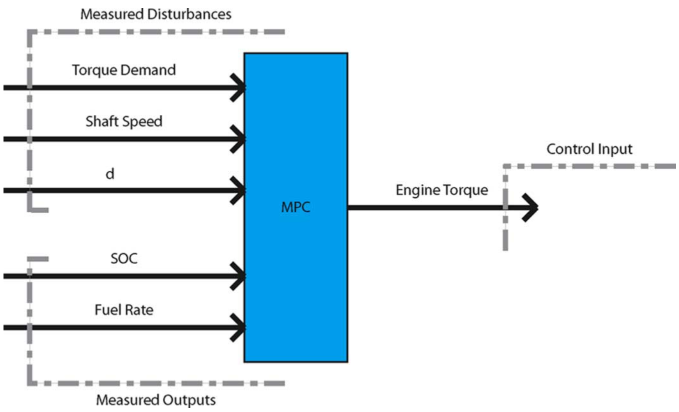

Fig. 21. Diagram of the signal structure of the MPC.

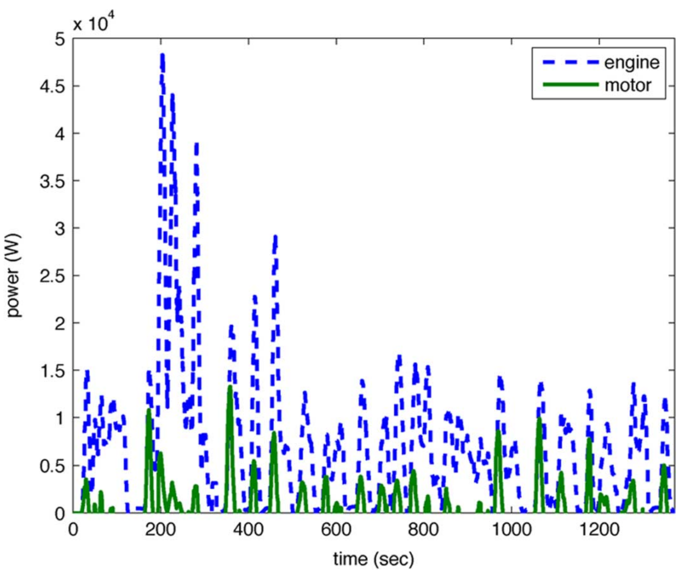

Fig. 22. Time history of motor and engine power with MPC on full-order model.

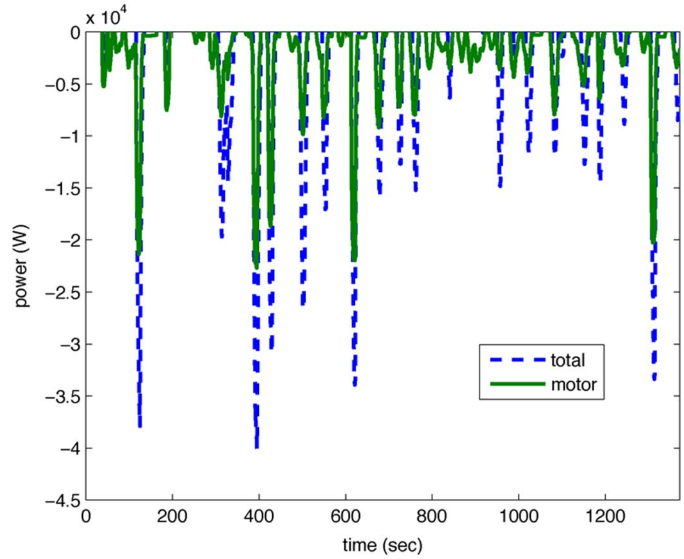

Fig. 23. Time history of the motor and friction brake power with MPC on full-order model.

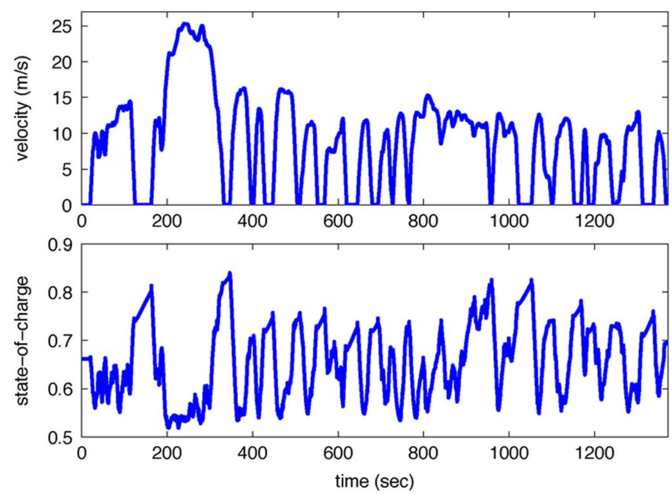

Fig. 24. Time history of velocity and soc with MPC on full-order model.

brakes are activated. Therefore, the rule-based strategy is used to control regeneration during negative power demand.

1) Simulation Results: The response of the linear model, at several candidate operating points, was compared to that of the parent nonlinear model. The operating point which resulted in the least amount of disparity was chosen for use in MPC design. This chosen operating point corresponds to a torque demand of $T_d = 41.9$ Nm and engine speed of $\omega_{\text{eng}} = 171.8$ rad/s. The operating points for engine torque is chosen at $T_{\text{eng}} = 31.9$ Nm and for battery state-of-charge we chose $\text{soc} = 0.9$. The fuel rate at this operating point is $\dot{m}_f = 5.87 \times 10^{-4}$ kg/s.

The closed-loop performance with MPC was studied under the UDDS cycle. The sampling interval of the MPC scheme was fixed to $\Delta t = 0.05$ seconds. The control horizon of $N = 1$ was found suitable and was fixed. The prediction horizon P, the state of charge reference soc_{ref}, and the penalty weights q_1, q_2, q_3 were tuned via various simulations to optimize the fuel economy. The final selection after several iterations was the following:

$$\text{soc}_{\text{ref}} = 0.5 \quad q_1 = 0.45 \quad q_2 = 250$$
$$q_3 = 0.004 \quad P = 100.$$

This final configuration of the model predictive controller applied to the nonlinear *reduced-order* plant model, was able to obtain a fuel economy increase of 8.9% over the $P_{\text{mot}} = 0$ case, outperforming the rule-based strategy by 3.9%, but still falling short of the DP-estimated 11.9% potential.

Next the MPC scheme was implemented on the nonlinear *full-order* model. Based on the earlier sizing experiments, the 40 kW motor and 78 F ultracapacitor were used in conjunction with the 160 kW engine. The design parameters which had been previously optimized using the reduced-order model were taken as an initial guess. With the penalty weights held fixed, the state-of-charge reference was varied to produce $\text{soc}_{\text{ref}} = 0.6$ as the most effective reference. Fixing the state-of-charge reference at this value, it became immediately apparent that the optimal weights from tuning on the reduced-order model were too far from their best values on the full-order model to provide a practical starting point. With this in mind, the original starting point was used, and the fuel rate penalty was varied with the other weights fixed at $q_1 = 1$ and $q_3 = 0$ to obtain $q_2 = 500$ as

TABLE III
DESCRIPTIONS OF VARIABLES USED IN FULL-ORDER MODEL

θ	Road Grade	R_{uc}	Line Resistance
ω_{eng}	Engine Speed	T_{air}	Air Temperature
$\omega_{in,gb}$	Gearbox Input Speed	$T_{cont,mot}$	Motor Continuous Torque
$\omega_{in,gb,filtered}$	Filtered Input Speed	T_{eng}	Engine Torque
$\omega_{in,tc}$	Torque Converter Input Speed	$T_{eng,out}$	Output Shaft Torque
ω_{mot}	Motor Speed	$T_{in,tc}$	Torque Converter Input Torque
ω_{ratio}	Torque Converter Speed Ratio	$T_{loss,gb}$	Gearbox Loss
$\omega_{out,gb}$	Gearbox Output Speed	$T_{loss,tc}$	Torque Converter Loss
$\omega_{out,tc}$	Torque Converter Output Speed	$T_{max,elec,mot}$	Electrical Torque Constraint
ω_w	Wheel Speed	$T_{max,eng}$	Maximum Engine Torque
C_{uc}	Capacitance	$T_{max,mech,mot}$	Mechanical Torque Constraint
F_{brake}	Friction Brake Force	$T_{min,eng}$	Minimum Engine Torque
F_{drag}	Drag Force	T_{mot}	Motor Torque
F_{grade}	Road Grade and Wheel Resistance Force	$T_{out,gb}$	Gearbox Output Torque
G_t	Gear Ratio	$T_{peak,mot}$	Motor Peak Torque
HI	Motor Heat Index	T_{uc}	Internal Temperature
$\dot{M}_{fuel}$	Fuel Consumption Rate	T_w	Wheel Torque
$P_{max,chg}$	Maximum Charging Power	$V_{out,uc}$	Output Voltage
$P_{max,dis}$	Maximum Discharging Power	$V_{uc,oc}$	Open-Circuit Voltage
$P_{max,mot}$	Maximum Electrical Power	g_f	Final Drive Ratio
P_{uc}	Electrical Power	i_{uc}	Current
$Q_{case,uc}$	Heat Transfer	q_{uc}	Charge
$Q_{gen,uc}$	Heat Generation	soc	State-Of-Charge
R_{chg}	Charging Line Resistance	v	Vehicle Velocity
R_{dis}	Discharging Line Resistance		

a better combination. From this point, the process was repeated to obtain $q_3 = 0.005$, followed by $q_2 = 50$. It is interesting to note that the previously obtained reference of $\mathrm{soc}_{\mathrm{ref}} = 0.6$ was still found to produce the most effective results, yielding

$$\mathrm{soc}_{\mathrm{ref}} = 0.6 \quad q_1 = 1 \quad q_2 = 50 \quad q_3 = 0.005 \quad P = 100$$

for the full-order model. With these control parameters, the full-order model was able to achieve a fuel economy increase of 13.1% over the conventional case. Time histories of this simulation are shown in Figs. 22–24. The MPC displays a much higher utilization of braking energy than that of the rule-based controller, owing to a lower state-of-charge at the beginning of each braking sequence. This fact is consistent with the controller's behavior during the tuning process, which resulted in a state-of-charge reference near the lower constraint of $\mathrm{soc} = 0.5$.

V. CONCLUSION

The mild ultracapacitor hybrid powertrain concept proposed in this study proved promising in improving the fuel economy of passenger vehicles in city driving without sacrificing drivability. After creating a detailed model of the powertrain, the potential for improvement was assessed in simulations using both rule-based and optimization-based control strategies. Various simulated component sizes and control strategies consistently indicate a potential for up to 15% improvement in fuel economy in city driving with the proposed mild hybrid powertrain. This order of improvement to fuel economy was confirmed by deterministic DP, which finds the optimal power management strategy numerically. This level of fuel economy improvement is below the projections in [3] for ultracapacitors, but still substantial and calls for further exploration into this technology. We have not explored the role of different powertrain configurations in this work, nor did we optimize the transmission shifting strategy; these remain areas to explore in the future.

TABLE IV
VALUES OF CONSTANT PARAMETERS USED IN FULL-ORDER MODEL

η_{uc}	0.9958	$P_{loss,eng}$	$700W$
μ_1	0.009	$R_{therm,uc}$	$0.8864\frac{K}{W}$
μ_2	0.00012	T_{inf}	$20C$
C	$0.6203\frac{kg}{m}$	$T_{loss,fd}$	$8Nm$
$C_{P,air}$	$1009\frac{j}{kg-K}$	$V_{min,uc}$	$3.7V$
$C_{P,uc}$	$1200\frac{j}{kg-K}$	$V_{max,uc}$	$92.5V$
J	$0.204kg-m^2$	g_f	3.27
$\dot{M}_{air}$	$0.014\frac{kg}{s}$	$i_{max,mot}$	$140A$
M	$2117.8kg$	r_w	$0.367m$
M_{uc}	$35.4645kg$	$\tau_{max,mot}$	$180s$

APPENDIX

See Tables III and IV.

ACKNOWLEDGMENT

The authors would like to thank Prof. J. Wagner of Clemson University for his valuable inputs on the project, and Dr. F. Leonardi and Dr. M. Jennings of Ford Motor Company for valuable discussions.

REFERENCES

[1] H. Douglas and P. Pillay, "Sizing ultracapacitors for hybrid electric vehicles," in *Proc. 31st Annu. Conf. IEEE Ind. Electron. Soc.*, 2005, pp. 1599–1604.
[2] G. Zurpette, "Supercharged," *IEEE Spectrum*, pp. 32–37, 2005.
[3] A. Burke, "Batteries and ultracapacitors for electric, hybrid, and fuel cell vehicles," *Proc. IEEE*, vol. 95, no. 4, pp. 806–820, Apr. 2007.
[4] W. Gao, "Performance comparison of a fuel cell-battery hybrid powertrain and a fuel cell-ultracapacitor hybrid powertrain," *IEEE Trans. Veh. Technol.*, vol. 54, no. 3, pp. 846–855, May 2005.

[5] W. Lajnef, J.-M. Vinessa, O. Briat, S. Azzopardi, and E. Woirgard, "Characterization methods and modelling of ultracapacitors for use as peak power sources," *J. Power Sources*, vol. 168, no. 2, pp. 553–560, 2007.

[6] B. Maher, "Ultracapacitors: The battery-less, high reliability backup solution," in *Proc. IEEE 27th Int. Telecommun. Conf.*, 2005, pp. 321–326.

[7] Z. Juda, "Ultracapacitors as an advanced energy source for braking energy recovery in electric vehicles," *Environment Protection Eng.*, vol. 32, pp. 195–202, 2006.

[8] M. Furubayashi, Y. Ushio, E. Okumura, T. Takeda, D. Andou, and H. Shibya, "Application of high power super capacitors to an idling stop system for city buses," in *Proc. 18th Int. Electric, Fuel Cell Hybrid Veh. Symp.*, 2001.

[9] J. Major, "Hybrid shuttle bus using ultracapacitors," in *Proc. Electr. Insulation Conf. Electr. Manuf. Expo.*, 2005, pp. 275–278.

[10] J. Anstrom, B. Zile, K. Smith, H. Hofmann, and A. Battra, "Simulation and field-testing of hybrid ultra-capacitor/battery energy storage systems for electric and hybrid-electric transit vehicles," in *Proc. IEEE Appl. Power Electron. Conf. Exposition*, 2005, pp. 491–497.

[11] A. Stienecker, T. Stuart, and C. Ashtiani, "A combined ultracapacitor—Lead acid battery energy storage system for mild hybrid electric vehicles," in *Proc. IEEE Veh. Power Propulsion Conf.*, 2005, pp. 1599–1604.

[12] A. Stienecker, T. Stuart, and C. Ashtiani, "An ultracapacitor circuit for reducing sulfation in lead acid batteries for mild hybrid electric vehicles," *J. Power Sources*, vol. 156, no. 2, pp. 755–762, 2006.

[13] L. Rosario and P. Luk, "Implementation of a modular power and energy management structure for battery-ultracapacitor powered electric vehicles," in *Proc. IET Hybrid Veh. Conf.*, 2006, pp. 141–156.

[14] P. Rodatz, O. Garcia, L. Guzzella, F. Buchi, M. Bartschi, A. Tsukada, P. Dietrich, R. Kotz, G. Scherer, and A. Wokaun, "Performance and operational characteristics of a hybrid vehicle powered by fuel cells and supercapacitors," SAE, Warrendale, PA, Paper 2003-01- 0418, 2003.

[15] R. Kotz, S. Muller, M. Bartschi, B. Schnyder, P. Dietrich, F. Buchi, A. Tsukada, G. Scherer, P. Rodatz, O. Garcia, P. Barrade, V. Hermann, and R. Gallay, "Supercapacitors for peak-power demand in fuel cell driven cars," *Electrochem. Soc. Proc.*, vol. 21, pp. 564–575, 2001.

[16] A. Vahidi, A. Stefanopoulou, and H. Peng, "Current management in a hybrid fuel cell power system: A model predictive control approach," *IEEE Trans. Control Syst. Technol.*, vol. 14, no. 6, pp. 1047–1057, Nov. 2006.

[17] P. Rodatz, G. Paganelli, A. Sciarretta, and L. Guzzella, "Optimal power management of an experimental fuel cell supercapacitor powered hybrid vehicle," *Control Eng. Practice*, vol. 13, pp. 41–53, 2005.

[18] A. Sciarretta and L. Guzzella, "Control of hybrid electric vehicles," *IEEE Control Syst. Mag.*, vol. 27, no. 2, pp. 60–70, Apr. 2007.

[19] Argonne National Laboratory, Argonne, IL, "Powertrain systems analysis toolkit," 2007. [Online]. Available: http://www.transportation.anl.gov/software/PSAT/index.html

[20] T. Minowa, H. Kimura, N. Ozaki, and M. Lbamoto, "Improvement of fuel consumption for a vehicle with an automatic transmission using driven power control with a powertrain model," *Soc. Autom. Eng. Japan (JSAE) Rev.*, vol. 17, pp. 375–380, Apr. 1996.

[21] T. Gillespie, *Fundamentals of Vehicle Dynamics*. Warrendale, PA: SAE International, 1992.

[22] A. Vahidi and W. Greenwell, "A decentralized model predictive control approach to power management of a fuel cell-ultracapacitor hybrid," in *Proc. Amer. Control Conf.*, 2007, pp. 5431–5437.

[23] W. Greenwell and A. Vahidi, "Experiments in predictive coordination of a fuel cell/ultracapacitor hybrid," in *Proc. ASME Dyn. Syst. Control Conf.*, 2008, pp. 119–126.

[24] D. Rotenberg, A. Vahidi, and I. Kolmanovsky, "Ultracapacitor assisted powertrains, modeling, control, sizing, and the impact on fuel economy," in *Proc. Amer. Control Conf.*, 2008, pp. 981–987.

[25] S. Delprat, J. Lauber, T. M. Guerra, and J. Rimaux, "Control of a parallel hybrid powertrain: Optimal control," *IEEE Trans. Veh. Technol.*, vol. 53, no. 3, pp. 872–881, May 2004.

[26] G. Paganelli, T. M. Guerra, S. Delprat, Y. Guezennec, and G. Rizzoni, "Optimal control theory applied to hybrid fuel cell powered vehicle," presented at the IFAC 15th Triennial World Congr., Barcelona, Spain, 2002.

[27] A. Sciarretta, M. Back, and L. Guzzella, "Optimal control of parallel hybrid electric vehicles," *IEEE Trans. Control Syst. Technol.*, vol. 12, no. 3, pp. 352–363, May 2004.

[28] C.-C. Lin, H. Peng, J.-M. Kang, and J. Grizzle, "Power management strategy for a parallel hybrid electric truck," *IEEE Trans. Control Syst. Technol.*, vol. 11, no. 6, pp. 839–849, Nov. 2003.

[29] I. Kolmanovsky, S. Sivashankar, and J. Sun, "Optimal control based powertrain feasibility assessment: A software implementation perspective," in *Proc. Amer. Control Conf.*, Portland, OR, Jun. 2005, pp. 4452–4457.

[30] M. M. Seron, G. C. Goodwin, and J. A. Dona, *Constrained Control and Estimation*. New York: Springer, 2005.

[31] A. Bemporad, "Model predictive control design: New trends and tools," in *Proc. IEEE Conf. Dec. Control*, 2006, pp. 6678–6683.

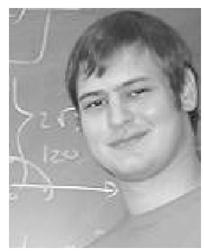

Dean Rotenberg received the B.S. degree in mechanical engineering with a minor in mathematics from Rose-Hulman Institute of Technology, Terre Haute, IN, in 2006, and the M.S. degree in mechanical engineering from Clemson University, Clemson, SC, in 2008.

He is currently working as an Analyst for the Department of Defense, Aberdeen Proving Ground, Aberdeen, MD, specializing in power and fuel consumption of military ground vehicles.

Ardalan Vahidi received the B.S. and M.S. degrees in civil engineering from Sharif University, Tehran, Iran, in 1996 and 1998, respectively, the second M.S. degree in transportation safety from George Washington University, Washington, DC, in 2002, and the Ph.D. degree in mechanical engineering from the University of Michigan, Ann Arbor, in 2005.

He is currently an Assistant Professor with the Department of Mechanical Engineering, Clemson University, Clemson, SC. His current research interests include optimization-based control methods and control of vehicular and energy systems.

Ilya Kolmanovsky (F'94) has received the M.S. and Ph.D. degrees in aerospace engineering and the M.A. degree in mathematics from the University of Michigan, Ann Arbor, in 1993, 1995, and 1995, respectively.

Before becoming a Professor with the Department of Aerospace Engineering, the University of Michigan, in 2010. He was with Ford Motor Company, where he was most recently a Technical Leader and a Manager of Modern Control Methods and Computational Intelligence group in Ford Research and Advanced Engineering. He has published over 200 refereed journal and conference articles on a spectrum of theoretical topics, and on a variety of automotive and aerospace control applications. He is named as an inventor on 78 U.S. patents.

Dr. Kolmanovsky was a recipient of several awards, including Donald P. Eckman Award of American Automatic Control Council and of IEEE Transactions on Control Systems Technology Outstanding Paper Award. He is a member of IEEE Control Systems Society Board of Governors.